J. Fluid Mech. (1996), *vol.* 306, *pp.* 1–30

Numerical simulations of uniformly stratified fluid flow over topography

By JAMES W. ROTTMAN[1], DAVE BROUTMAN[2] AND ROGER GRIMSHAW[3]

[1] Praxis, Inc., 6080 Franconia Road, Alexandria, VA 22310, USA and E. O. Hulburt Center for Space Sciences, Naval Research Laboratory, Washington DC 20375, USA

[2] Department of Applied Mathematics, University of New South Wales, Sydney, NSW 2052, Australia

[3] Department of Mathematics, Monash University, Clayton, VIC 3168, Australia

(Received 17 October 1994 and in revised form 7 July 1995)

We use a high-resolution spectral numerical scheme to solve the two-dimensional equations of motion for the flow of a uniformly stratified Boussinesq fluid over isolated bottom topography in a channel of finite depth. The focus is on topography of small to moderate amplitude and slope and for conditions such that the flow is near linear resonance of either of the first two internal wave modes. The results are compared with existing inviscid theories: the steady hydrostatic analysis of Long (1955), time-dependent linear long-wave theory, and the fully nonlinear, weakly dispersive resonant theory of Grimshaw & Yi (1991). For the latter, we use a spectral numerical technique, with improved accuracy over previously used methods, to solve the approximate evolution equation for the amplitude of the resonant mode. Also, we present some new results on the modal similarity of the solutions of Long and of Grimshaw & Yi. For flow conditions close to linear resonance, solutions of Grimshaw & Yi's evolution equation compare very well with our fully nonlinear numerical solutions, except for very steep topography. For flow conditions between the first two resonances, Long's steady solution is approached asymptotically in time when the slope of the topography is sufficiently small. For steeper topography, the flow remains unsteady. This unsteadiness is manifested very clearly as periodic oscillations in the drag, which have been observed in previous numerical simulations and tow-tank experiments. We explain these oscillations as mainly due to the internal waves that according to linear theory persist longest in the neighbourhood of the topography.

1. Introduction

The flow of a uniformly stratified inviscid Boussinesq fluid over two-dimensional localized bottom topography in a channel of finite depth has been the subject of extensive study since the pioneering work of Long (1955). For this special but important class of flows, Long derived a linear field equation (often called Long's equation) that describes the fully nonlinear steady flow with the assumption that all the streamlines originate upstream (i.e. no closed streamlines). Long found solutions that obey this assumption, provided that the flow is not close to resonance. Near resonance closed streamlines appear, suggesting that no steady solution exists and that internal wave-breaking may occur. Solutions of the linear initial-value problem show that at resonance the topography forces an internal wave mode that grows indefinitely with

time (linearly with time in the hydrostatic limit), so that even very small topography eventually gives rise to large-amplitude internal waves and nonlinear behaviour.

Grimshaw & Smyth (1986) derived an approximate evolution equation that describes the weakly nonlinear evolution of the amplitude of the upstream component of the resonant mode for arbitrary stable stratification and uniform mean flow. The evolution equation they obtained is the forced Kortweg de Vries (fKdV) equation and is based on the assumption that, for topography of small amplitude and moderate slope, a balance is achieved between weak nonlinearity and linear dispersion. This balance implies that the flow response to the introduction of the topography scales as the square root of the amplitude of the topography. The theory fails, however, for the special case of uniform stratification (the case of interest here) because the nonlinear terms vanish and therefore cannot balance the dispersion: this failure occurs because the fully nonlinear steady-state flow is governed by a linear field equation.

Grimshaw & Yi (1991; hereinafter referred to as GY) proposed an approximate theory for resonant flow in uniformly stratified flows. They derived a new evolution equation, which we will refer to as the finite-amplitude long-wave equation (or more simply, the FLW equation), that is a small perturbation of a time-dependent form of Long's equation, based on the assumptions that the flow is near resonance and the time development is very slow. They assumed that, for topography of small amplitude and moderate slope, the upstream propagating component of the resonant mode has an amplitude that scales with the channel depth and that the nonlinearity comes in through the time dependence which scales with the $\frac{3}{2}$ power of the amplitude of the topography. Thus topography, no matter how small, will produce near resonance a response of the order of the channel depth, but the smaller the topography the longer it will take for this large-amplitude response to develop. The FLW equation has the property, shared with Long's equation, that the solutions are valid only up to the point where overturning streamlines appear somewhere in the flow. That is, the FLW equation can describe everything up to but not including breaking internal waves.

Although there have been some recent studies by Hanazaki (1992, 1993) and Lamb (1994) that compare the results of numerical solutions of the fully nonlinear equations with those of the FLW equation for a few cases, there is as yet no thorough study of the range of validity of the FLW equation. In particular, these previous studies concentrated on relatively narrow obstacles. Furthermore, it appears that previous numerical solutions of the FLW equation did not accurately take into account singularities that occur in the FLW equation's kernel function. We find that these singularities become significant as breaking amplitudes are approached. In the present work we describe the results of a systematic study of this problem over a range of obstacle amplitudes and slopes using a high-resolution spectral method to solve the fully nonlinear inviscid equations for a Boussinesq fluid and an improved numerical method to solve the FLW equation.

In §2 we define the problem and review Long's hydrostatic steady theory, linear hydrostatic resonant theory and GY's weakly dispersive resonant theory. This review contains what we believe are some new insights into the self-similar behaviour of these theories. In §3 we outline the numerical methods we used for solving the fully nonlinear inviscid equations and the methods we used to solve the FLW equation. In §4 we describe our numerical results. In §5, we summarize and conclude.

2. Review of the theory

2.1. *Governing equations*

The flow and coordinate system under consideration are sketched in figure 1. We use a Cartesian coordinate system with x as the horizontal and z as the vertical coordinate. A stratified, incompressible and inviscid fluid with constant buoyancy frequency N flows through a channel of total depth D that is bounded above by a horizontal rigid lid and below by a two-dimensional surface-mounted obstacle represented by the curve $z = h(x)$. We will assume that $h(x)$ is positive, symmetric and streamlined, with maximum height a and half-width L and such that $h(x) \to 0$ as $x \to \pm\infty$. The density variation of the fluid over the depth of the channel is assumed to be sufficiently small compared to the mean density $\bar{\rho}_0$ of the fluid for the Boussinesq approximation to be accurate.

We consider the two-dimensional motion that results from an initial condition corresponding to an idealized tow-tank experiment. That is, at time $t = 0$ surfaces of constant density are all horizontal and the fluid is at rest, and at time $t = 0^+$ the obstacle is impulsively accelerated to a constant speed U. We seek the solutions of this problem for $t > 0$ in a reference frame in which the obstacle is at rest (as depicted in figure 1). Accordingly, we choose a background state to consist of a constant horizontal speed U and horizontally homogeneous density $\rho_0(z)$ and pressure $p_0(z)$ that satisfy the hydrostatic condition $\mathrm{d}p_0/\mathrm{d}z = -g\rho_0$, where g is the acceleration due to gravity.

The equations of motion in the Boussinesq approximation are

$$\frac{\partial u}{\partial x} + \frac{\partial w}{\partial z} = 0, \tag{2.1}$$

$$\frac{\mathrm{d}u}{\mathrm{d}t} = -\frac{1}{\bar{\rho}_0}\frac{\partial p}{\partial x}, \tag{2.2}$$

$$\frac{\mathrm{d}w}{\mathrm{d}t} = -\frac{1}{\bar{\rho}_0}\frac{\partial p}{\partial z} - g(\rho - \rho_0)/\bar{\rho}_0, \tag{2.3}$$

$$\frac{\mathrm{d}\rho}{\mathrm{d}t} = 0, \tag{2.4}$$

where

$$\frac{\mathrm{d}}{\mathrm{d}t} = \frac{\partial}{\partial t} + (U+u)\frac{\partial}{\partial x} + w\frac{\partial}{\partial z}, \tag{2.5}$$

and u, w are the horizontal and vertical components of the perturbation velocity (the velocity relative to the background flow), ρ is the density and p is the dynamic pressure.

For mathematical convenience, we introduce the perturbation streamfunction $\psi(x, z, t)$, defined as

$$u = -\frac{\partial \psi}{\partial z}, \quad w = \frac{\partial \psi}{\partial x}, \tag{2.6}$$

and the vorticity $\omega(x, z, t)$, defined such that,

$$\omega = \frac{\partial w}{\partial x} - \frac{\partial u}{\partial z} = \nabla^2 \psi. \tag{2.7}$$

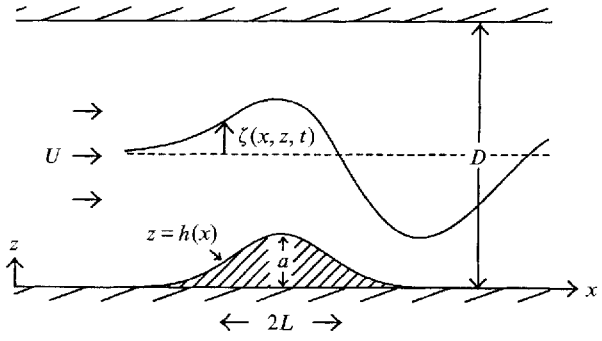

FIGURE 1. A schematic diagram of the flow under consideration.

Also, it is useful in the following discussion to introduce the vertical displacement $\zeta(x,z,t)$, which is defined such that the density is given by $\rho(x,z,t)=\rho_0(z-\zeta)$ and solves (2.4) exactly provided that

$$\frac{\mathrm{d}\zeta}{\mathrm{d}t}=\frac{\partial\psi}{\partial x}. \tag{2.8}$$

Finally, we can eliminate the pressure from (2.2) and (2.3) to obtain the single equation

$$\frac{\mathrm{d}\omega}{\mathrm{d}t}=-N^2\frac{\partial\zeta}{\partial x}, \tag{2.9}$$

in which the buoyancy frequency N is given by

$$N^2=-\frac{g}{\bar{\rho}_0}\frac{\mathrm{d}\rho_0}{\mathrm{d}z}, \tag{2.10}$$

and is assumed here to be a constant. Thus, the problem can be reformulated so that there are three unknowns ζ, ψ, and ω given by the three equations (2.7), (2.8), and (2.9).

The boundary conditions are

$$\psi=Uh(x) \quad \text{on} \quad z=h(x), \tag{2.11}$$

$$\psi=0 \quad \text{on} \quad z=D, \tag{2.12}$$

which ensures that the component of fluid velocity normal to the bounding surfaces is zero, and the initial conditions corresponding to an impulsively accelerated obstacle are given by

$$\zeta(x,z,0)=0 \tag{2.13}$$

$$\omega(x,z,0)=0. \tag{2.14}$$

Another idealized initial condition that is common in analyses of flow over topography is to assume that the obstacle is 'pushed up' impulsively from an initially flat lower boundary. This alternative initial condition is expressed by (2.11)–(2.14) as above except that (2.13) is replaced by a different and more complicated expression which if linearized reduces to $\zeta(x,z,0)=\psi(x,z,0)/U$. These different initial conditions will affect mainly the form of the transients, and will have little or no effect on the long-time behaviour of the flow near the obstacle.

In all the simulations described in this paper the specific obstacle shape used was

$$h(x)=a\exp[-(x-x_0)^2/L^2], \tag{2.15}$$

in which x_0 is the location of the obstacle crest. Given a particular obstacle shape, there are three non-dimensional parameters that define this problem:

$$\frac{a}{D}, \quad \frac{L}{D}, \quad K = \frac{ND}{\pi U}, \tag{2.16}$$

where K is the inverse Froude number (the ratio of the fastest linear internal gravity wave speed in the channel to the mean fluid speed). The resonant points are where $K = n$, with $n = 1, 2, \ldots$. We will focus our attention on (but not entirely restrict it to) small to moderate values of a/D, moderate to large values of L/D and $1 \leqslant K \leqslant 2$. In general we will present our results in terms of the vertical displacement $\zeta(x, z, t)$.

In the following discussion of the inviscid theories, we will focus for simplicity on obstacles with sufficiently large L/D such that the hydrostatic approximation is valid.

2.2. *Long's model for steady flow*

First, we seek steady solutions of the problem posed in the previous section. For this situation Long (1955) derived a now well-known linear field equation that describes the fully nonlinear flow field which can be thought of as a generalization of potential flow to a restricted class of stratified flows. For obstacles that have sufficiently long horizontal extent for the hydrostatic approximation to be applicable, this equation can be written as

$$\frac{\partial^2 \zeta}{\partial z^2} + \frac{N^2}{U^2}\zeta = 0. \tag{2.17}$$

For steady flows ζ is related to the perturbation streamfunction by

$$\zeta = \psi / U. \tag{2.18}$$

The exact solution of (2.17) that satisfies boundary conditions (2.11) and (2.12) is

$$\zeta = h(x)\frac{\sin[K\pi(1 - z/D)]}{\sin[K\pi(1 - h(x)/D)]}. \tag{2.19}$$

Long's model is derived based on the assumption that all streamlines originate upstream and therefore that there are no regions of the flow containing closed streamlines (regions of recirculating flow). Long showed that (2.19) satisfies this assumption in the following regions of the parameter space: (*a*) for $H = a/D$ that satisfies $0 \leqslant H < 1$ (that is, all physically valid values of H) if $K < 1$, and (*b*) for H that satisfies

$$K\pi H - |\sin[K\pi(1 - H)]| \leqslant 0, \tag{2.20}$$

if $K \geqslant 1$. Otherwise, apparently no physically valid steady solutions exist, since the solutions of Long's model produce statically unstable flows that presumably imply the existence of wave breaking and associated unsteadiness. More details of the properties of (2.19) are described by Baines & Guest (1988). We have plotted the curve produced by (2.20) when the equality holds (which we will refer to as the breaking curve) in the $K - H$ parameter space in figure 2. This curve separates regions of steady flow from unsteady flow, based on Long's model. Regions where no steady flow exists are shown shaded in the figure.

There are several interesting features about the parameter space diagram in figure 2. First, when $K < 1$ (where the flow is supercritical to all linear wave modes in the

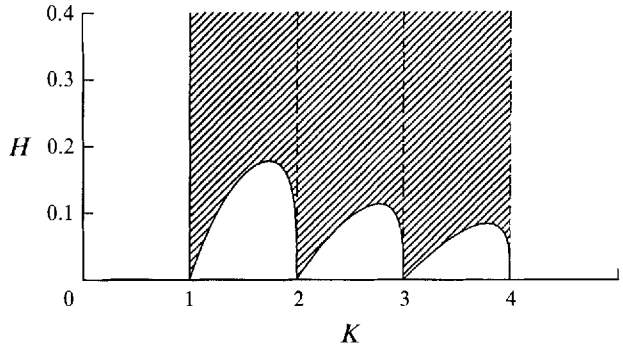

FIGURE 2. The $K-H$ parameter space diagram for the hydrostatic Long's model solution of flow over a two-dimensional obstacle for $0 \leqslant K \leqslant 4$. The unshaded areas are regions of the parameter space for which the solution satisfies the assumptions used in deriving Long's model and the shaded regions are where the solution contains closed recirculating cells (which violate the assumptions used in deriving the model).

channel) physically valid steady solutions exist for all possible obstacle amplitudes. Secondly, and conversely, when $K = n$ (where $n = 1, 2, \ldots$) there are no obstacle heights for which steady solutions exist. These are the points at which one of the linear long gravity wave modes is resonant in the channel. Thirdly, for small H the region of unsteady flow near $K = n$ is not symmetric. For $K < n$ (where the flow is supercritical with respect to mode n) the curve that separates steady from unsteady flow approaches the $H = 0$ axis very steeply and for small $(n-K)$ has the form

$$H = \frac{1}{K}\left(\frac{6}{\pi^2}\right)^{1/3}(n-K)^{1/3} \tag{2.21}$$

(for all n except $n = 1$, which is a special case where the boundary curve is a vertical line). For $K > n$ (where the flow is subcritical with respect to mode n) the curve approaches the $H = 0$ axis more slowly and for small $(K-n)$ has the form

$$H = \frac{1}{K}\frac{1}{2}(K-n). \tag{2.22}$$

Fourthly, the mean value of H that satisfies (2.20) when equality holds decreases as K increases such that H seems to scale as $1/K$.

This last point suggests that when $K \geqslant 1$ a more natural vertical lengthscale is $\pi U/N$. This new scale is related to the vertical wavelength of the linear long waves that can exist in the channel when $K \geqslant 1$. When $K = 1$ one mode can exist in the channel and its half vertical wavelength equals D. As K increases above 1, more linear modes can exist in the channel and these modes have progressively smaller half vertical wavelengths, the smallest being equal to D/n, where n is the largest integer less than K. With this scaling we can show that the curve represented by (2.20) when the equality holds is similar for $K \geqslant 1$. We define non-dimensional variables, denoted by superscript * as

$$H^* = KH, \quad K^* = K-n+1, \tag{2.23}$$

where $n = 1, 2, \ldots$ is chosen such that $K^* = K$ if $K < 2$ and $1 \leqslant K^* < 2$ if $K \geqslant 2$. Then (2.20) can be written as

$$\pi H^* - |\sin[\pi(K^*-H^*)]| \leqslant 0. \tag{2.24}$$

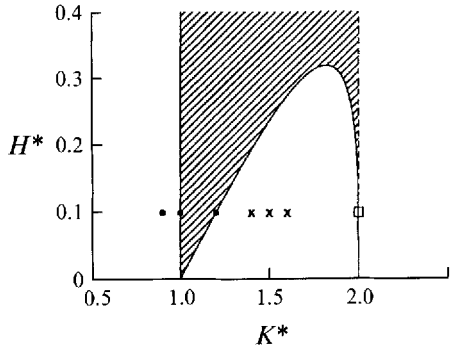

FIGURE 3. The K^*-H^* parameter space diagram for the hydrostatic Long's model solution for flow over two-dimensional obstacles. The unshaded and shaded regions have the same meaning as in figure 2. ●, cases plotted in figures 8 and 9; ×, cases plotted in figures 15 and 17; □, cases plotted in figures 20 and 21.

Therefore, this scaling collapses the curves for all the regions $n \leqslant K < n+1$, for $n = 2, 3, \ldots$, onto the region $1 \leqslant K < 2$. We have plotted (2.24) in figure 3. Note that the maximum obstacle amplitude for which steady solutions exist when $K > 1$ is $KH = 1/\pi \approx 0.32$, which is a good measure of when the obstacle amplitude is large enough to induce strongly nonlinear or overturning flow.

For obstacles with horizontal lengthscales that are not large enough for the hydrostatic approximation to be valid, the form of the breaking curves are a function of the shape of the obstacle and must be determined numerically. Long (1955) computed these breaking curves for obstacles with a range of horizontal lengthscales (although he did not specify the exact shapes of these obstacles) and his results indicate that the general form of the breaking curves is similar to (2.20) but that the amplitude of the curve increases as the horizontal scale of the obstacle decreases. This increase in amplitude can be as much as 50% over the hydrostatic value when the horizontal scale of the obstacle asymptotes to zero.

There have been no experimental or numerical experiments to verify the form of this breaking curve for obstacles with shallow slopes. However, there has been an experimental attempt, Baines (1977), as well as an inviscid numerical attempt, Lamb (1994), to verify the breaking curves for obstacles with small horizontal scales (a Witch of Agnesi shape with ratios of obstacle half-widths to channel depths of between 0.13 to 0.3). Neither could reproduce the theoretical breaking curves. They found that, in general, wave breaking occurred below the theoretical curves, except near the resonance points. At resonance, the experiments showed no wave breaking, whereas the numerical simulations seemed to show wave breaking where Long's model indicates it should occur but only after a long time (which may have been too long for breaking to be observed during the course of the experiments). Interestingly, although breaking was observed to occur below the theoretical breaking curve corresponding to the horizontal lengthscale of these narrow obstacles, breaking was never observed to occur below the hydrostatic breaking curve.

2.3. *Linear theory for unsteady flow*

If we assume that the obstacle is small and its horizontal lengthscale large, and furthermore that the response of the fluid to the introduction of the obstacle into the flow is proportional to the amplitude of the obstacle, then the governing equations

(2.7)–(2.9), to lowest order in the obstacle amplitude, can be reduced to the following equation for ζ

$$\left(\frac{\partial}{\partial t}+U\frac{\partial}{\partial x}\right)^2\frac{\partial^2\zeta}{\partial z^2}+N^2\frac{\partial^2\zeta}{\partial x^2}=0. \tag{2.25}$$

The boundary and initial conditions for this problem are the linearized hydrostatic forms of (2.11)–(2.14). These can be expressed as

$$\frac{\partial\zeta}{\partial t}+U\frac{\partial\zeta}{\partial x}=U\frac{\mathrm{d}h}{\mathrm{d}x} \quad \text{on} \quad z=0, \tag{2.26}$$

$$\zeta(x, D, t)=0, \tag{2.27}$$

and

$$\zeta(x, z, 0)=0, \tag{2.28}$$

$$\frac{\partial\zeta}{\partial t}=U\frac{\mathrm{d}h}{\mathrm{d}x}(1-z/D) \quad \text{at} \quad t=0. \tag{2.29}$$

An identical equation and analogous boundary and initial conditions can be derived for ψ. Using standard Laplace and Fourier transform methods, we find that the solution of (2.25) when $K \neq n$ can be expressed as

$$\zeta(x,z,t)=h(x)\frac{\sin[\pi K(1-z/D)]}{\sin(\pi K)} - U\sum_{m=1}^{\infty}\left[\frac{h(x-(U+c_m)t)}{U+c_m}+\frac{h(x-(U-c_m)t)}{U-c_m}\right]\frac{\sin(m\pi z/D)}{m\pi} \tag{2.30}$$

where

$$c_m=\frac{ND}{m\pi} \tag{2.31}$$

is the long-wave phase and group speed for the mode m. This solution has a steady part and a transient part. The steady part clearly is an approximation to (2.19) that is valid for small $h(x)$. The transient part consists of a sum over all the linear long-wave modes with each mode having two components, one that propagates against the oncoming flow and another that propagates with it. All these transients have the horizontal structure of the obstacle and propagate away from the obstacle as time increases. If $c_m < U$, then the flow is supercritical with respect to mode m and both transients will be downstream of the obstacle and if $c_m > U$, then the flow is subcritical with respect to mode m and the transient that propagates against the current will be upstream of the obstacle. As long as $K \neq n$ the steady solution is approached near the obstacle as $t \to \infty$.

If $c_m = U$ for some $m = n$, say, then $K = n$ and the flow is critical with respect to mode n. In the limit as $K \to n$ (2.30) becomes

$$\zeta(x,z,t)=\frac{Ut}{n\pi}\frac{\mathrm{d}h}{\mathrm{d}x}\sin\left(\frac{n\pi z}{D}\right)+h(x)(1-z/D)\cos\left(\frac{n\pi z}{D}\right)+\text{transients}, \tag{2.32}$$

where the transients are the same as in the corresponding non-resonant expression except with the singular term (containing the denominator $U-c_n$) excluded. (Note that when (2.30) and (2.32) are decomposed into individual sine modes they do not agree with GY's (2.18) and (2.19). GY's linear solutions correspond to the initial conditions for an impulsively 'pushed up' obstacle and not for an impulsively accelerated flow.) The amplitude of the component of mode n that is stationary with respect to the

obstacle increases linearly with time. So (2.32) is valid for early times only. For times greater than $Ut/D \sim n\pi L/D$, which implies $\zeta \sim a$, the assumption that the flow response scales with the obstacle amplitude clearly is invalid. However, since $L \gg D$ by assumption, linear resonant theory may be valid for a substantial period of time.

Linear resonant theory can be used to estimate the time when wave overturning will occur when $K \approx n$. If we assume that wave overturning occurs when $\zeta \sim D/n\pi$, for reasons described in the previous section, then based on linear resonant theory this wave breaking time should scale as $Ut/D \sim L/a$. However, it would seem unlikely that linear theory would remain valid all the way up to the time of wave breaking.

2.4. *The GY model for resonant flow*

When the flow conditions are such that one of the modes is resonant, then as shown by (2.32) the component of the solution that propagates against the mean flow has an amplitude that grows linearly with time. Eventually, the amplitude of this mode will become large enough to invalidate the assumption that the flow response is proportional to the obstacle amplitude, although the amplitudes of the steady and downstream propagating components of this mode and all the components of the remaining (non-resonant) modes will remain linear for small enough obstacle amplitudes. A new scaling is required when the upstream propagating mode becomes nonlinear.

Grimshaw & Yi (1991) develop a theory to describe the growth of the resonant mode for obstacles of small amplitude and moderate slopes. They assume that the vertical displacement of the fluid scales with the channel depth and that the time scale of the development of the flow scales with the slope of the obstacle (which is consistent with linear resonant theory). They make the additional assumption that the obstable follows the KdV relationship between the vertical and horizontal lengthscales: $a/D \sim (D/L)^2$. These latter two assumptions imply that the flow develops with a time that scales as $(D/U)(a/D)^{-3/2}$. The use of the KdV scaling restricts the validity of the theory to obstacles that have a certain aspect ratio: the smaller the obstacle the larger its horizontal lengthscale must be for the theory to remain valid.

Using the above scaling relationships, GY use a multi-scale perturbation expansion to obtain an approximate evolution equation for the amplitude of the resonant mode, which is in essence a time-dependent form of Long's equation. In terms of the vertical displacement and assuming that the nth mode is the resonant mode GY express the upstream propagating component of this mode as

$$\zeta(x, z, t) \sim A(x, t) \sin(n\pi z/D), \tag{2.33}$$

which is related to the perturbation streamfunction in this case by

$$\zeta \sim \psi/c_n, \tag{2.34}$$

and the amplitude function A is governed by the following evolution equation, which we will call the FLW equation,

$$\int_{-\infty}^{x} G(A, A') \frac{\partial A'}{\partial t} \mathrm{d}x' + (U - c_n) A - \frac{1}{2} \frac{c_n^3}{N^2} \frac{\partial^2 A}{\partial x^2} - \frac{c_n^2}{ND} \left(1 - \frac{N}{c_n} A\right) h = 0, \tag{2.35}$$

where $A = A(x, t)$, $A' = A(x', t)$ and the kernel function $G(A, A')$ is given by

$$G(A, A') = \frac{1}{D} \int_0^D \left\{ \frac{\partial z}{\partial A} \frac{\partial z'}{\partial A'} - z \frac{\partial z}{\partial A} \frac{\partial^2 z'}{\partial \xi \partial A'} - z' \frac{\partial z'}{\partial A'} \frac{\partial^2 z}{\partial \xi \partial A} \right\} \mathrm{d}\xi. \tag{2.36}$$

The variable ξ is defined as

$$\xi = z - A(x, t) \sin(n\pi z/D), \tag{2.37}$$

from which the inverse relationships $z = z(\xi, A)$ and $z' = z(\xi, A')$ can be derived. For these inverse relationships to be single valued, we must require

$$|A| < \frac{D}{n\pi} = \frac{c_n}{N}, \tag{2.38}$$

which is equivalent to requiring that there are no overturning streamlines in the flow or that the perturbation horizontal fluid speed nowhere equals or exceeds the mean speed, the same restriction imposed on Long's model. It should be remembered that (2.38) is an approximate criterion for overturning flow since it represents only the upstream propagating component of the resonant mode. For strongly nonlinear and dispersive flows other modes may contribute to cause overturning streamlines to occur earlier or later than predicted by (2.38). The evolution equation derived by GY allows for small variations of the background stability profiles from uniform stability which results in an additional term in (2.35) that has basically an A^2 dependence, but since we are concentrating on strictly uniform stratification we have neglected this term.

The evolution equation (2.35) should be solved with initial conditions obtained by matching with the linear solution (2.32) for times during which both the linear and weakly nonlinear solutions are valid. For the case of an impulsively accelerated flow this matching procedure gives $A(x, 0) = 0$. Incidentally, we get the same initial condition for the case of an obstacle that is impulsively 'pushed up', since the matching occurs with the resonant part of the linear solution which is the same in both cases.

The kernel function $G(A, A')$ given by (2.36) appears to be a rather daunting obstacle to the efficient numerical solution of the FLW equation. However, G is a function only of A and A', both of which are strictly limited by (2.38), so a table of G values can be computed at the beginning of the calculation and values needed during the course of the time integration can be obtained efficiently by interpolation. Moreover, the table of G values needs to be computed only for one mode, since a straightforward but tedious calculation shows that the mode number n can be removed from G by scaling all the vertical lengths by D/n. So, the values of G for any mode can be obtained from the values of G calculated for, say, mode 1 simply by rescaling A and A'.

Indeed, the mode number n can be eliminated from the entire FLW equation if the vertical lengths are scaled by D/n, the horizontal lengths by $D/n^{1/2}$ and the time by $n^{1/2}D/U$. Thus, a numerical solution of the FLW equation for, say, mode 1 can be rescaled to obtain a solution for any other mode. The usefulness of this similarity property of the FLW equation is diminished by the fact that the solution at the new mode number is not for the same obstacle, but for an obstacle whose height is reduced by a factor of n and whose horizontal lengthscale is reduced by a factor of $n^{1/2}$.

3. Numerical methods

3.1. *The spectral model*

We use a spectral collocation method (Canuto *et al.* 1988; Boyd 1989) to solve the equations of motion in their vorticity-streamfunction form, as expressed in (2.7)–(2.9) with boundary conditions (2.11) and (2.12). A Fourier series is used in the horizontal direction (typically with 256 collocation points), and Chebyshev series in the vertical (typically with 40 or 65 points). An absorbing (and periodic) sponge layer is added at both lateral boundaries of the computational domain, covering about $\frac{1}{16}$ of the computational domain on each side. We found that there was negligible reflection from the downstream sponge layer, but significant reflection from the upstream one.

Therefore we always placed our obstacle in the computational domain such that any disturbances would not reach the upstream sponge layer during the duration of the computation.

In the vertical direction, we removed the obstacle from the lower boundary condition by transforming the equations to terrain-following coordinates (X, Z) defined as

$$X = x, \quad Z = D\left[\frac{z-h(x)}{D-h(x)}\right], \tag{3.1}$$

such that in the computational domain the flow is confined between two parallel horizontal boundaries at $Z = 0$ and $Z = D$. To compare with the results of the FLW equation, the vertical displacement computed using the spectral method was expanded in a sine series. Since in general ζ is not zero on the lower boundary, as required for any numerical evaluation of a finite sine series, we actually found the sine transform of the related function:

$$\zeta(X, Z, t) - \zeta(X, 0, t)(1 - Z/D) = \sum_{m=1}^{\infty} A_m(x, t) \sin(m\pi Z/D). \tag{3.2}$$

Sufficiently far from the obstacle $h \approx 0$, then $\zeta(X, 0, t) \approx 0$, and $A_m(x, t)$ can be identified as the amplitude function of the mth normal mode.

A third- or fourth-order Runge–Kutta scheme is used to timestep the equations. We use the low-storage version of Runge–Kutta described by Canuto *et al.* (1988) that has good numerical stability properties. The elliptic equation (2.7) is solved using an iterative technique. This approach is based on a direct method that Canuto *et al.* (1988) refer to as a matrix-diagonalization scheme. Since we have used a non-conformal mapping to terrain-following coordinates, this direct method is only approximate, and we use iteration to refine the solution. Typically, four or five iterations were sufficient to achieve the desired accuracy.

Wave overturning or breaking occurs over a wide range of the parameter space in this study. We define the onset of wave breaking as when the vertical derivative of the density first vanishes, or equivalently in terms of the vertical displacement when

$$\frac{\partial \zeta}{\partial z} = 1, \tag{3.3}$$

anywhere in the flow. We call the time at which this occurs the wave breaking time t_{br} since it is when an isopycnal becomes vertical and if the wave continues to develop will result in the isopycnal overturning.

Wave breaking, as well as some anomalies associated with the impulsively accelerated obstacle initial conditions (to be discussed in more detail in the next section), generate small-scale disturbances that are not resolved by our model and lead to aliasing errors and eventually numerical instability. To eliminate these difficulties we employ a high-order high-wavenumber filter in both the horizontal and vertical directions. This procedure allowed us to compute a numerically stable solution well past the time at which constant density surfaces overturned.

The drag on the obstacle is given by

$$\text{drag} = \int_{-\infty}^{\infty} P \frac{\mathrm{d}h}{\mathrm{d}x} \mathrm{d}x, \tag{3.4}$$

where P is the pressure on the lower boundary. We computed this quantity by first integrating (3.4) by parts, evaluating the x-derivative of the pressure from the horizontal momentum equation and finally using the trapezoidal rule to perform the integration over the length of the computational domain.

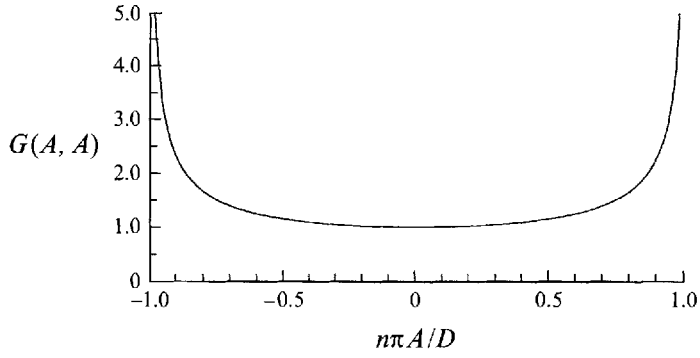

FIGURE 4. A plot of the FLW equation kernel function $G(A, A)$ as a function of A for mode n waves.

3.2. *The GY model*

The FLW equation was solved numerically using essentially the method described by GY and Yi & Warn (1987). The key step of this method is to differentiate (2.35) with respect to x to obtain the following integral equation for $\partial A/\partial t$:

$$G(A,A)\frac{\partial A}{\partial t}+\frac{\partial A}{\partial x}\int_{-\infty}^{x}\frac{\partial G(A,A')}{\partial A}\frac{\partial A'}{\partial t}\,\mathrm{d}x' = -(U-c_n)\frac{\partial A}{\partial x}+\frac{1}{2}\frac{c_n^3}{N^2}\frac{\partial^3 A}{\partial x^3}+\frac{c_n^2}{ND}\left[\left(1-\frac{N}{c_n}\frac{\partial A}{\partial x}\right)h-\frac{N}{c_n}\frac{\mathrm{d}h}{\mathrm{d}x}\right]. \quad (3.5)$$

This is a Volterra integral equation of the second kind whereas (2.35) is a Volterra integral equation of the first kind. Equation (3.5) is preferred because the inversion of Volterra integral equations of the second kind is numerically stable whereas the inversion of equations of the first kind is not. We note in passing that except for the form of the time dependence (3.5) bears a close resemblance to the forced KdV equation.

As in the spectral model, we assume that the motion is periodic in x with period equal to the length of the computational domain and insert 'sponge' layers at the two computational boundaries. The spatial derivatives are evaluated spectrally by expanding A in a Fourier series in x. A standard fourth-order quadrature-type scheme is used to solve (3.5) for $\partial A/\partial t$ and then A is advanced in time using the same third-order Runge–Kutta scheme as used in the spectral model. This scheme did not require any filtering or smoothing to keep it stable.

To increase the speed of the calculation, the functions $G(A, A)$ and $\partial G(A, A')/\partial A$ were evaluated in advance on a uniform grid over the domain $-D/n\pi < A, A' < D/n\pi$ and needed values were obtained during the course of the time integration by interpolation. For all the calculations presented here we used a grid of 128 points for both A and A'. Figures 4 and 5 are plots of these functions as they were used in the solution of (3.5). In general these functions are very well behaved except in the neighbourhood of the maximum allowed amplitudes, when (2.38) is an equality, where both functions have singularities. These singularities, which have not been noted by previous investigators, must be treated very carefully as the flow approaches breaking amplitude. We ensured that we adequately resolved these singularities by checking for consistency with increased resolution and by checking wave breaking times with the fully nonlinear model.

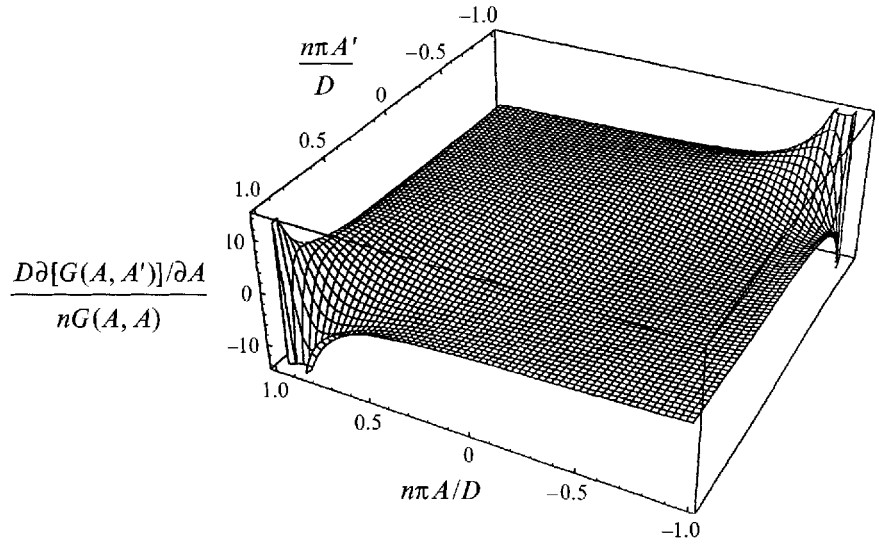

FIGURE 5. A surface plot of the function $[G(A,A)]^{-1}\partial G(A,A')/\partial A$ as a function of A and A' for mode n waves.

For the FLW equation, we define the wave breaking time t_{br} as when (2.38) is first violated. In computing the wave-breaking time, errors due to inadequate resolution of the singularity in the kernel function are most noticeable at linear resonance, since the wave-breaking amplitude is approached very slowly in this case and any small error will produce premature breaking. As an example, we compare our numerical solution of the FLW equation with GY's solution for the case shown in GY's figure 9(*a*) (which corresponds to $K = 1$, $a/D = 0.1$ and $L/D = 1.33$). GY computed breaking to occur when $Ut/D \approx 11$, whereas we obtained $Ut/D \approx 156$ and the fully nonlinear model gives $Ut/D \approx 276$. (We comment that this is a particularly difficult case for computing the breaking time, because the vertical displacement increases initially very rapidly to near breaking amplitude but then its growth rate slows such that the final small-amplitude increase needed to achieve breaking is approached very slowly. Therefore, even small errors in this final but long-time approach to breaking amplitude will lead to premature breaking.)

An expression for the drag on the obstacle that is consistent with the approximations made in deriving the FLW equation is

$$\text{drag} = \int_{-\infty}^{\infty} \left[\bar{\rho}_0 c_n^2 \frac{n\pi}{D} A\left(1 - \frac{1}{2}\frac{n\pi}{D}A\right)\right]\frac{\mathrm{d}h}{\mathrm{d}x}\mathrm{d}x, \tag{3.6}$$

where the quantity in square brackets is the pressure at $z = 0$. We computed this integral using a fourth-order quadrature rule over the length of the computational domain.

4. Results

4.1. *Initial conditions*

Our initial conditions, which mimic what is done in laboratory tow-tank experiments, lead to some difficulties for our inviscid and non-diffusive spectral model. For an impulsively accelerated flow the isopycnal surfaces initially are horizontal and

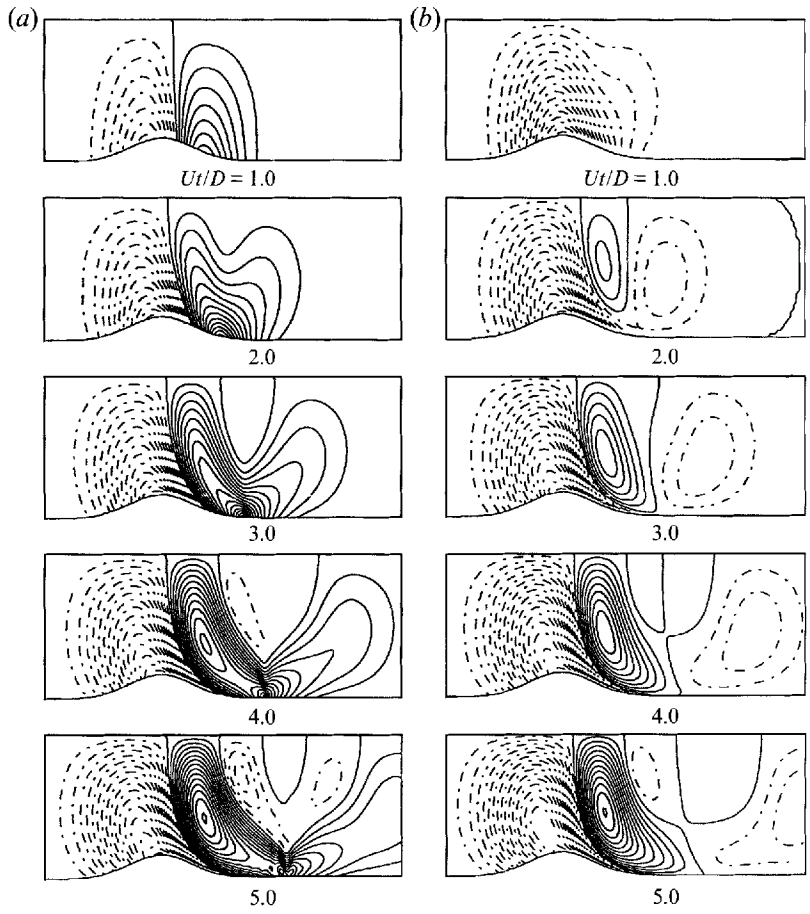

FIGURE 6. Contour plots of perturbation density for two types of initial conditions at the times $Ut/D = 1.0$, 2.0, 3.0, 4.0 and 5.0. The parameter values for these plots are, $Ka/D = 0.2$, $L/D = 2.0$ and $K = 1.2$. Each plot shows the entire depth but only a small region near the obstacle of the length of the computational domain. ---, positive perturbations; ——, negative perturbations: (*a*) impulsively accelerated flow, and (*b*) impulsively 'pushed-up' obstacle.

therefore several of them intersect the obstacle surface. Since the fluid particles initially on the obstacle surface cannot leave that surface, a small region with a horizontal density gradient is generated along the bottom boundary when the initial non-uniform distribution of density is swept over the obstacle crest after the flow is initiated. This small blob of non-uniform density is advected downstream by the mean flow and with time this density gradient sharpens continuously as the heavier fluid advances into the lighter fluid. Since there is no diffusion in our formulation, there is nothing to stop this density gradient from getting ever more sharp. Such a sharp gradient is very difficult to resolve numerically and eventually, if spectral filtering is not used, saturates the spectrum and leads to a breakdown of the calculation. This small abnormality can be seen propagating downstream at the mean flow speed in all of our spectral simulations. The alternative initial conditions in which the obstacle is 'pushed up' impulsively at the beginning does not produce this problem since the density is always uniform on the obstacle surface.

Figure 6 illustrates the differences in these two types of initial conditions. Figure 6(*a*) is a series of contour plots of the perturbation density for the early time motion of an

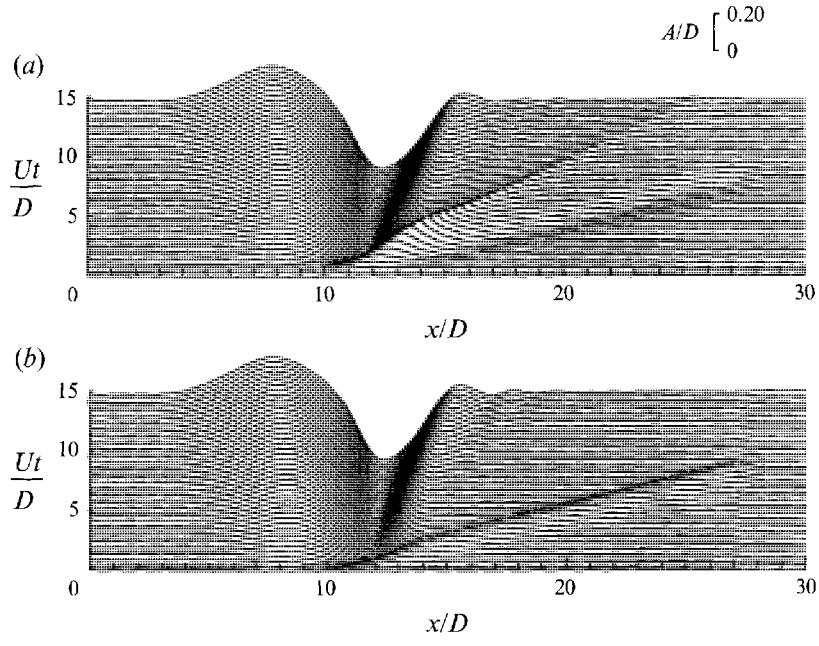

FIGURE 7. The amplitude function $A(x, t)$ for the resonant mode of vertical displacement as computed by the spectral model for the case with, $Ka/D = 0.2$, $L/D = 2.0$ and $K = 1.2$ corresponding to the cases shown in figure 6. The obstacle is centred at $x/D = 10$: (*a*) impulsively accelerated flow, and (*b*) impulsively 'pushed-up' obstacle.

impulsively accelerated flow, and figure 6(*b*) is a similar series for the case of an impulsively 'pushed-up' obstacle (actually, we used the linearized form of the initial condition corresponding to the obstacle being 'pushed up' impulsively, as described in §(2.1)). The flow patterns shown in figure 6 for these two cases are very similar after $Ut/D \approx 2$, except for the obvious small contracting blob of negative perturbation density in the impulsively accelerated flow. This blob can be seen propagating at the mean flow speed along the bottom surface downstream of the obstacle in figure 6(*a*). By $Ut/D \approx 4$ this small blob has contracted into a very tight knot, and the calculation could not be continued much beyond this time unless the spectral filter was introduced to prevent further tightening. The 'pushed-up' obstacle initial condition had none of these problems, as can be seen in figure 6(*b*).

Another look at this initial density anomaly is provided by the plots of time evolution of $A(x, t)$ shown in figure 7. For the impulsively accelerated flow (figure 7*a*) two disturbances can be seen propagating rapidly downstream. The fastest disturbance is a small wave of depression that propagates faster than the mean flow speed. This is the mode 1 transient that propagates in the direction of the mean flow. The other downstream propagating disturbance is a positive anomaly that propagates with the mean flow speed. This is the density anomaly described above. This density anomaly is seen in all the modes, showing that it is a very broadband disturbance. For the impulsively 'pushed-up' obstacle (figure 7*b*) the only disturbance seen propagating downstream is the mode 1 wave transient. In this case, the transient is a wave of elevation.

Even though the 'pushed-up' obstacle is a 'cleaner' type of initial condition, we chose to use the impulsively accelerated initial condition because it more closely resembles the initial conditions used in laboratory tow-tank experiments. Of course, in

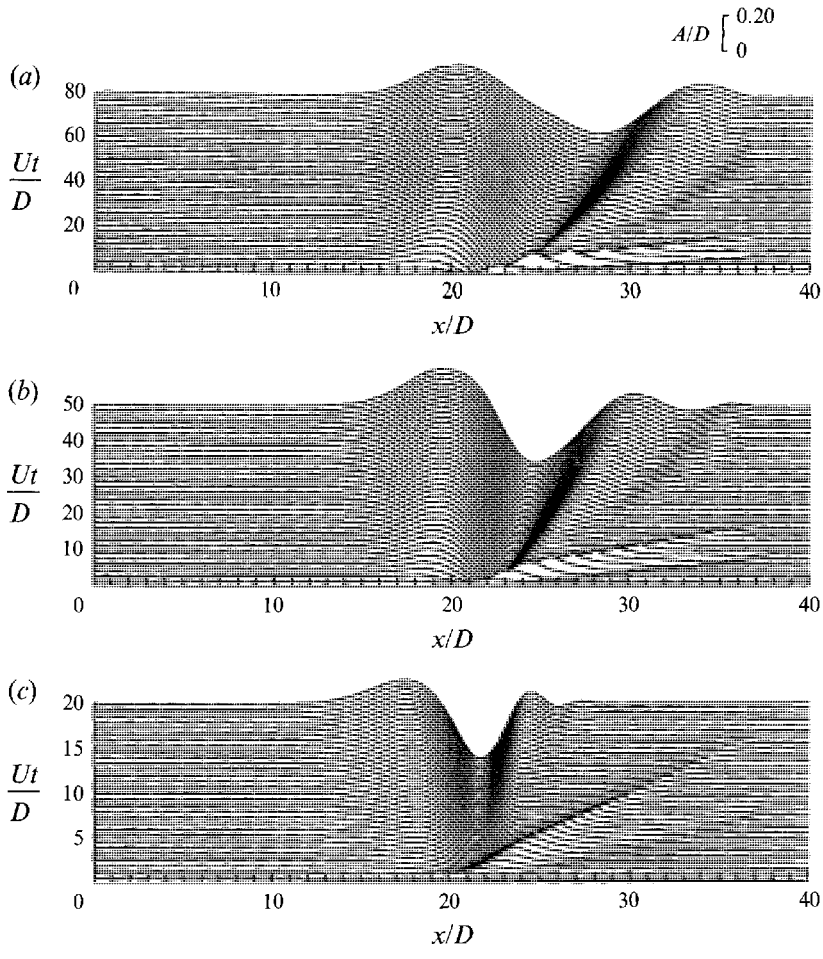

FIGURE 8. The amplitude function $A(x, t)$ for the resonant mode of the vertical displacement as computed by the spectral model for the cases with $Ka/D = 0.1$, $L/D = 2.0$, and (*a*) $K = 0.95$, (*b*) $K = 1.00$, and (*c*) $K = 1.20$. The obstacle is centred at $x/D = 20$.

the laboratory experiments this type of anomaly will be diminished by such real fluid effects as viscosity and diffusion. In our numerical simulations we successfully controlled the density anomaly with spectral filtering.

4.2. *The first resonance point* ($K = 1$)

In this section we describe our results for the parameter space in the vicinity of the first resonant point at $K = 1$. Using both the spectral model and the FLW equation, we performed calculations for about 50 different combinations of the flow parameters. Specifically, the ranges of the flow parameters for which we performed calculations were: $0.05 < Ka/D \leqslant 0.2$, $0.25 \leqslant L/D \leqslant 8.0$ and $0.95 \leqslant K \leqslant 1/(1-2a/D)$. The maximum value of K used in this range defines the subcritical boundary of the resonance region, as given by (2.22). In our calculations we fixed Ka/D and varied K, since, as discussed previously, Ka/D is a more appropriate measure of nonlinearity than is a/D. We note that for $L/D \geqslant 2$ we observed breaking only within the regions of the parameter space delineated by the hydrostatic breaking curve (2.20).

The evolution in time of the amplitude function $A(x, t)$ for the resonant mode as computed by the spectral model is plotted in figure 8 and by the GY model in figure

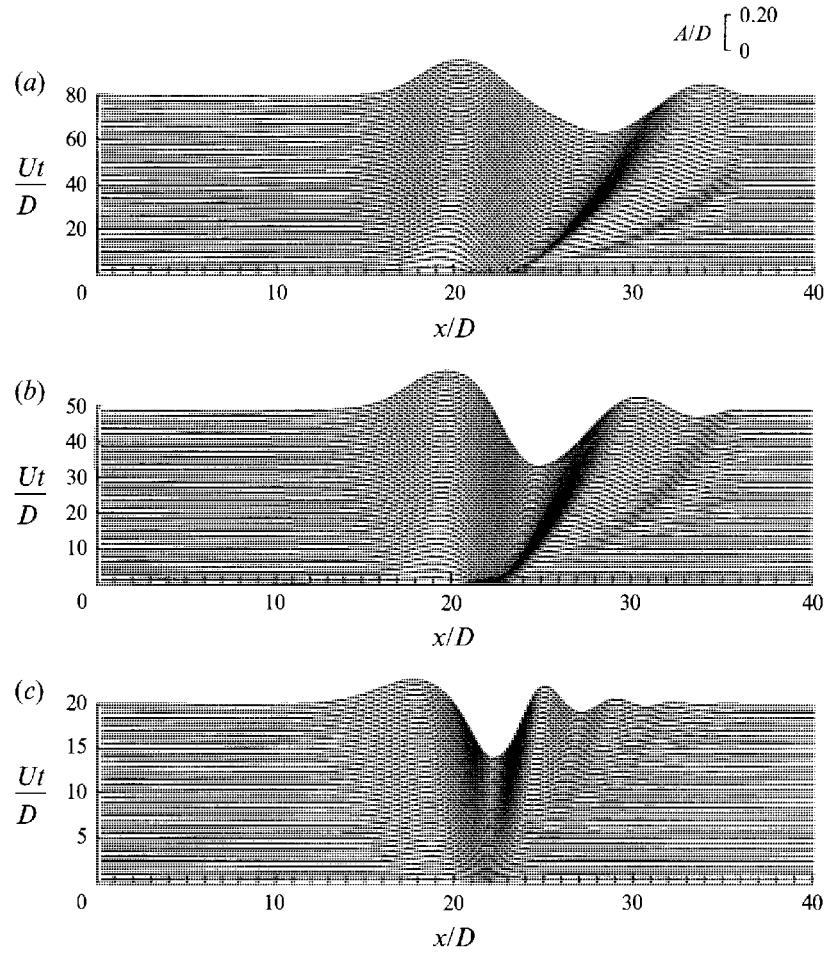

FIGURE 9. The amplitude function $A(x, t)$ for the resonant mode of the vertical displacement as computed by the GY model for the cases with $Ka/D = 0.1$, $L/D = 2.0$, and (*a*) $K = 0.95$, (*b*) $K = 1.00$ and (*c*) $K = 1.20$. The obstacle is centred at $x/D = 20$.

9 for the three cases with $Ka/D = 0.1$, $L/D = 2.0$, and $K = 0.95$, 1.00 and 1.20. These cases, which are plotted as ● in the parameter space shown in figure 3, were chosen as representative flows for obstacles of moderate amplitude and slope. The results shown in both figures 8 and 9 have been computed up to the wave-breaking time as calculated from the GY model, except for the case with $K = 0.95$ for which the flow approaches a steady state and there is no breaking. These wave-breaking times, as well as the horizontal positions where breaking occurs, are listed in table 1. Note that for these cases the GY model always underestimates the spectral model breaking time by about 25% to 30%. Otherwise, apart from the already discussed start-up transient, which of course does not appear in the GY model, the two sets of computed amplitude functions are qualitatively and quantitatively nearly identical.

The plots in figures 8(*a*) and 9(*a*) show that for the case with $K = 0.95$ the crest that develops directly over the obstacle has reached a constant amplitude by $Ut/D \approx 15$ and the flow downstream is detaching from the flow directly over the obstacle, eventually leaving a symmetrical bulge over the obstacle, which is characteristic of steady supercritical flows. For $K = 1.0$ a crest again develops directly over the obstacle but the

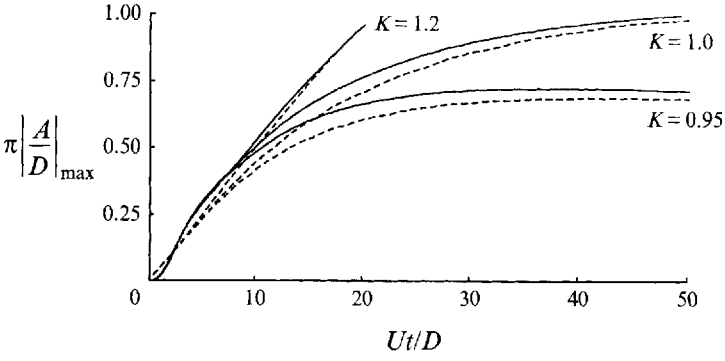

FIGURE 10. A plot of $|A(x_{br}, t)|$ as a function of time corresponding to the calculations shown in figures 8 and 9, where x_{br} is the horizontal position at which wave breaking first occurs: ——, spectral model; – – –, GY model. A value of $|A| \geqslant D/\pi$ indicates wave breaking in the GY model.

K	Ut_{br}/D	$(x_{br}-x_0)/D$
0.95	* (*)	* (*)
1.00	79 (50)	4.4 (4.7)
1.05	35 (28)	2.8 (3.2)
1.10	31 (24)	2.2 (2.5)
1.20	27 (21)	1.4 (1.9)

TABLE 1. The time t_{br} and horizontal position x_{br} of wave breaking for the spectral model calculations shown in figure 8. The values in parentheses were obtained from the GY model calculations shown in figure 9. In these calculations $Ka/D = 0.1$, and $L/D = 2.0$. The obstacle is centred at x_0 and note that for the obstacle shape used the horizontal position of maximum slope is $(x-x_0)/D = \pm(L/D)/\sqrt{2} \approx \pm 1.4$. The symbol * means that no wave-breaking occurred.

first downstream trough steadily deepens, rapidly at first and more slowly later, until it reaches breaking amplitude. Since the amplitude function is negative where it reaches breaking amplitude, we can deduce from (2.33) and (3.3) that the vertical position of breaking must be located at the upper boundary. For $K = 1.20$, the development of the flow to breaking amplitude is similar to the $K = 1.0$ case, except that the flow develops more rapidly and the crest that develops over the obstacle starts to propagate upstream.

The absolute value of A at a fixed location downstream (where breaking first occurs) is plotted as a function of time in figure 10 for the cases corresponding to those plotted in figures 8 and 9. The solid lines show the results for the spectral model and the dashed lines for the GY model. For the cases in which wave breaking occurs, we have plotted these lines up to the time this is predicted by the GY model (which as shown in table 1 is always less than the time predicted by the spectral model). For times up to $Ut/D \approx 10$ the amplitude in all these cases increases nearly linearly with time as predicted by linear resonant theory. For later times the deviation from linear growth is a function of K. For $K = 0.95$ the growth stops altogether, for $K = 1.0$ the growth becomes very slow but yet still eventually reaches breaking amplitude, and for $K > 1$ the growth is faster the larger the value of K. In fact for $K = 1.20$ the growth is nearly linear all the way to breaking. Note that the amplitude of the resonant mode calculated from the spectral model is always greater than that from the GY model even though the GY model reaches breaking amplitude sooner. This indicates that higher modes

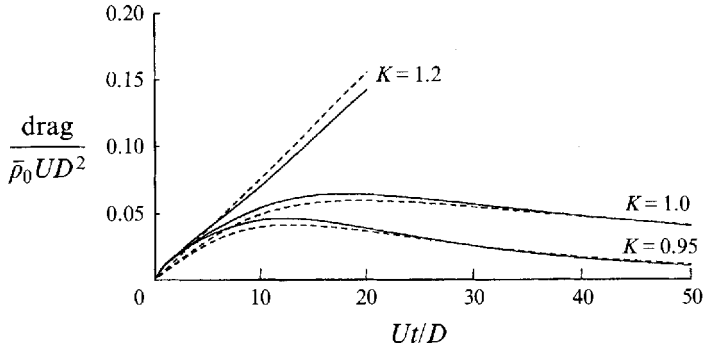

FIGURE 11. A plot of the drag as a function of time corresponding to the calculations shown in figures 8 and 9: ——, spectral model; – – –, GY model.

(mostly the second mode) tend to inhibit breaking as the amplitude increases and delays the onset of breaking in the spectral model. Otherwise the two models are qualitatively very similar. The FLW equation does a good job of reproducing the time-dependent behaviour of the full spectral model.

The conclusion that the FLW equation represents the full calculation well is reinforced by the drag (an integral measure of the flow) computed from the two models and plotted in figure 11. Again, the spectral results are plotted as solid lines and the GY model results as dashed lines. The two methods produce very similar results, with the GY model slightly under-predicting the drag except when $K = 1.2$ for which it slightly over-predicts the drag. These results show that for $K = 0.95$ the drag asymptotically approaches zero, indicating that the flow eventually becomes symmetric about the obstacle. For $K \geqslant 1.00$ the drag is non-zero when breaking occurs and the indications are that the drag remains non-zero after breaking. This implies that the flow in the neighbourhood of the obstacle is approaching a permanent asymmetrical form with high pressure on the upstream surface and lower pressure on the downstream surface.

Figure 12 shows a time sequence of density contour plots computed by the spectral model for the case with $Ka/D = 0.1$, $L/D = 2.0$ and $K = 1.2$. These plots show how the whole flow field would look in the laboratory for times after the obstacle is accelerated to a constant speed. Note the development of the deep trough downstream of the crest that breaks at the horizontal position near the maximum slope of the obstacle and at the vertical position near the upper boundary just after $Ut/D \approx 25$. Also note the rapid development of a crest over the obstacle, and that this crest eventually propagates upstream. After the initial breaking the trough begins to widen and the next crest downstream begins to increase in amplitude and eventually also breaks, but this time the breaking occurs near the bottom boundary. In all of our numerical experiments wave breaking occurred downstream of the obstacle crest.

So far we have presented the results for an obstacle that we have described as of moderate amplitude and moderate slope. For higher amplitudes, we found that the flow looks much the same as we have shown above except that the flow develops more rapidly. Narrower obstacles produce more horizontal structure downstream and a different dependence of the breaking time on obstacle dimensions. This is illustrated in figure 13, for $K = 1.2$ and $Ka/D = 0.1$ and 0.2. For large fixed L/D the breaking times are simply inversely proportional to a/D, but for small fixed L/D the breaking times appear to be inversely proportional to $(a/D)^3$. For fixed a/D, the breaking times show

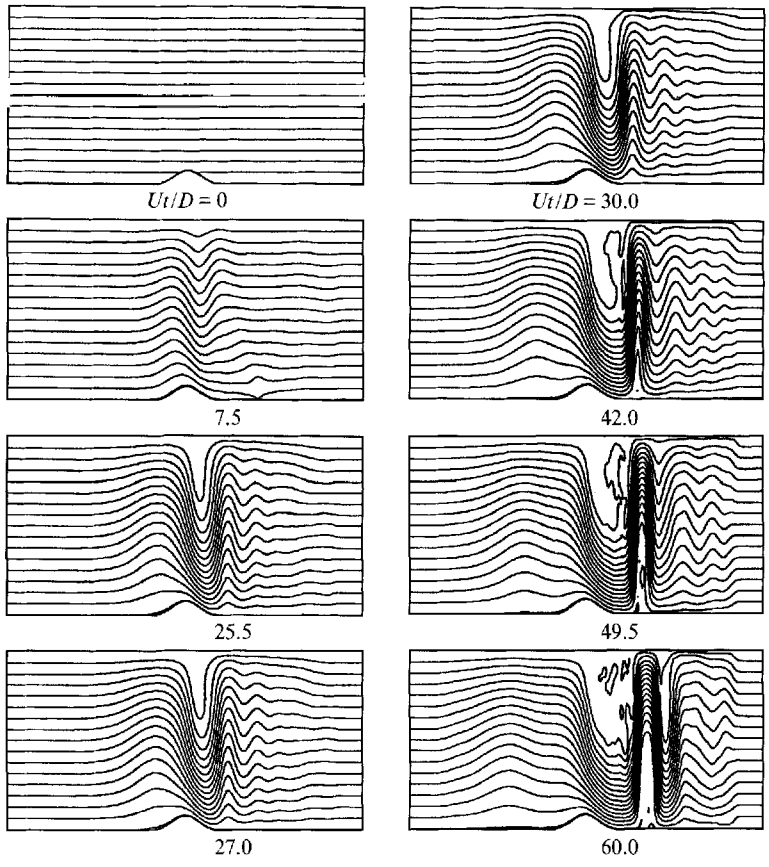

FIGURE 12. Contour plots of the density field as computed by the spectral model for the case with $Ka/D = 0.1$, $L/D = 2.0$ and $K = 1.2$. The domain length is $40D$ and the contour interval is $\Delta\rho/\bar{\rho}_0 = 0.0025$. In this case, breaking occurred at $Ut/D \approx 27$.

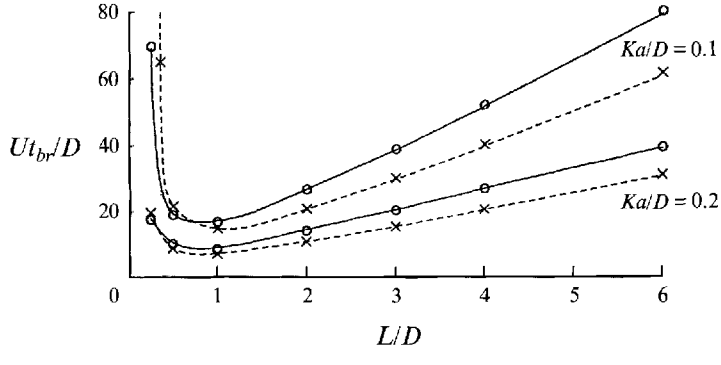

FIGURE 13. The breaking time as a function of L/D for $Ka/D = 0.1$ and 0.2 and $K = 1.2$: ——, spectral model; – – –, GY model.

the interesting behaviour that they are large for both large and small L/D and have a minimum near $L/D \approx 1.0$. More specifically, for large L/D the breaking times are simply proportional to L/D, whereas for small L/D the breaking times are inversely proportional to $(L/D)^3$.

The above results suggest that with fixed K and $L/D \gg 1$ the breaking times t_{br} scale as $Ut_{br}/D \sim L/a$, which is the scaling for the resonant mode as predicted by linear

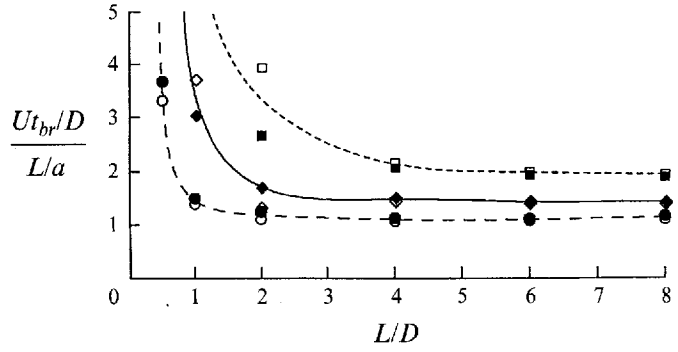

FIGURE 14. The non-dimensional breaking time, scaled by L/a, as computed by the spectral model as a function of L/D. The open symbols are for $Ka/D = 0.1$ and the solid symbols for $Ka/D = 0.2$: □ and ■, $K = 1.0$; ◇ and ◆, $K = 1.05$; ○ and ●, $K = 1.2$. The curves are subjective fits to the data: ------, $K = 1.0$; ——, $K = 1.05$; – – –, $K = 1.2$.

hydrostatic theory; see (2.32). Figure 14 shows that this scaling is valid for $KL/D > 3$, and in this regime the data is well represented by the empirical formula:

$$Ut_{br}/D = (1+e^{-\beta(K-n)})\frac{L}{a}, \tag{4.1}$$

with $n = 1$ and $\beta \approx 11.0$. Furthermore, (4.1) is a good fit to the breaking time computed by the GY model if it is multiplied by approximately 0.75. Note from table 1 that the FLW equation very accurately predicts the horizontal position at which wave breaking first occurs.

For $L/D \ll 1$ a stationary phase approximation to the non-hydrostatic linear resonant solution suggests that the breaking times should scale as $Ut_{br}/D \sim (a/D)^{-3}(L/D)^{-3}$, which compares well with our limited number of results for $L/D \leqslant 0.5$.

Figure 13 shows that there is some variation in the agreement between the breaking times computed by the spectral model and the GY model with obstacle amplitude and slope. We find that the GY model over-predicts this time for small L/D and under-predicts it for large L/D. Hence, there is an intermediate range of L/D over which the GY model predicts a breaking time that agrees quite well with that computed by the spectral model. The value of L/D where the GY model is most accurate varies with the obstacle amplitude and we find empirically from a limited data set that it appears to follow the relationship

$$\frac{L}{D} = f(K)\left(\frac{a}{D}\right)^{-1/2}, \tag{4.2}$$

where $f(K)$ is some (as yet not fully determined) function of K. This is of course the assumed scaling relationship in the FLW equation. If the obstacle satisfies (4.2) then the FLW equation agrees very well with the spectral model even for relatively large obstacle amplitudes, but even if the obstacle does not satisfy (4.2) the results of the FLW equation are generally qualitatively in agreement with the spectral model and for obstacles with moderate to low slopes is at least within 25%, or so, of the spectral model results.

Hanazaki (1992, 1993) made a series of comparisons between numerical solutions of the full Navier–Stokes equations for moderate to large Reynolds numbers and numerical solutions of the FLW equation for a range of values of K similar to what we

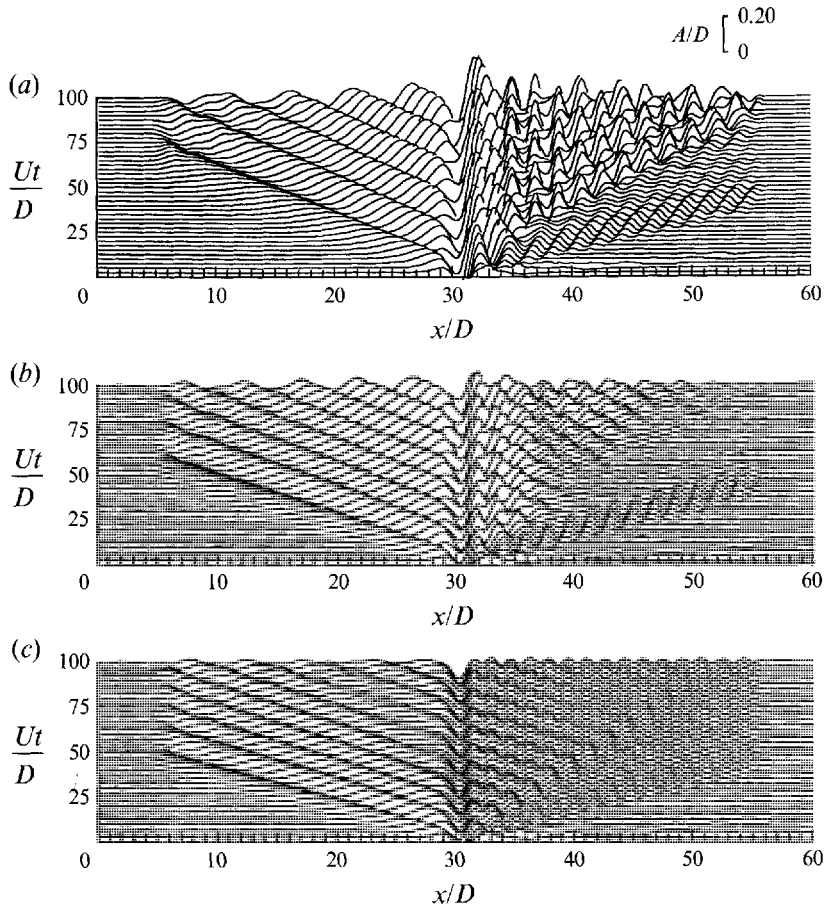

FIGURE 15. The amplitude function $A(x, t)$ for the first mode of the vertical displacement as computed by the spectral model for the cases with $Ka/D = 0.1$, $L/D = 1.0$, and (*a*) $K = 1.4$, (*b*) $K = 1.5$ and (*c*) $K = 1.6$. The obstacle is centred at $x/D = 30$.

have done here. All of his calculations were for obstacles with $L/D = 0.25$, and as we have shown this horizontal scale falls in the narrow-obstacle regime. Hanazaki found good qualitative comparison between the GY model and his fully nonlinear model, but he made few quantitative comparisons of such things as the time to wave breaking. With obstacles of such small horizontal scale we would expect these times to be quite large, and in fact Hanazaki's fully nonlinear calculations do not show any signs of breaking up to $Ut/D = 200$, which is the time at which he terminates his calculations. In only one calculation ($K = 1.05$ and $a/D = 0.15$) did Hanazaki's numerical solution of the GY model predict wave breaking, which occurred at $Ut/D = 57$. We computed this case with our numerical method of solving the GY model and obtained wave breaking at $Ut/D = 87$. We attribute the difference to our more careful treatment of the kernel singularity.

Lamb (1994) compared the breaking times from two of his numerical solutions of the fully nonlinear inviscid equations with the breaking times computed by GY. The two cases are for $K = 1.05$, $a/D = 0.04$, $L/D = 2.12$ and $K = 1.21$, $a/D = 0.14$, $L/D = 1.14$. Lamb's fully nonlinear model gave the breaking times for these two cases as $Ut/D \approx 82$ and $Ut/D \approx 13.5$, respectively, whereas GY found $Ut/D \approx 36$ and $Ut/D \approx 5$. Actually, these two cases are derived from one calculation done in GY

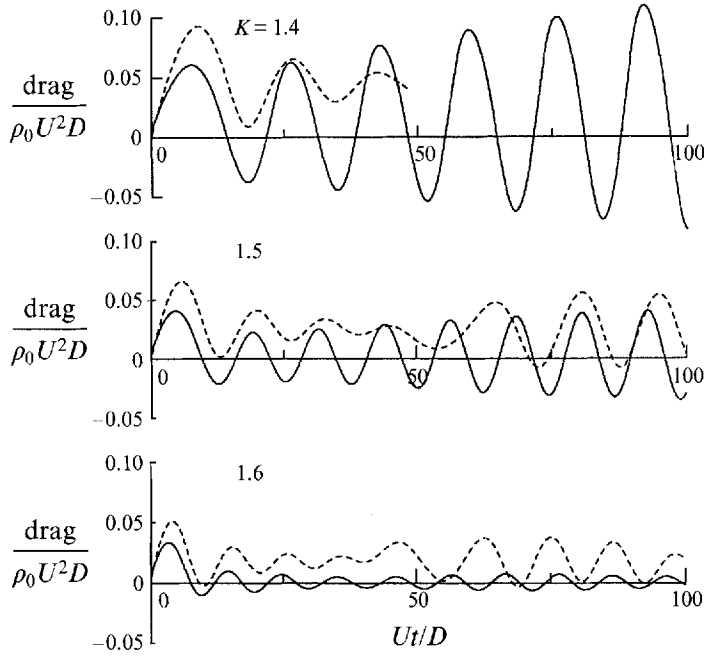

FIGURE 16. A plot of the drag as a function of time for the case with $K = 1.4$, 1.5 and 1.6, corresponding to the calculations shown in figures 15: ——, spectral model; – – –, GY model. The GY curves are plotted up to the time that wave breaking occurs in this model.

(shown in their figure 10*a*) by rescaling the original non-dimensional results. We computed these two cases with our numerical implementation of the GY model and obtained the breaking times of $Ut/D \approx 65$ and $Ut/D \approx 9$, respectively. Again we attribute the discrepancies between our results and GY's results to our more careful treatment of the kernel singularity near breaking amplitudes.

4.3. *The approach to Long's steady solution* ($1 < K < 2$)

We now consider the region of the parameter space shown in figure 3 where we would expect to obtain valid steady solutions of Long's model. In figure 15, we show the amplitude function $A(x, t)$ for mode 1 waves as computed by the spectral model for three cases with $Ka/D = 0.1$, $L/D = 1.0$ and $K = 1.4$, 1.5 and 1.6. All of these three cases, which are plotted as $\times$ symbols in the parameter space shown in figure 3, should be well within the region where there are valid steady solutions, yet even up to $Ut/D = 100$ the solutions do not appear to be approaching a steady state. Instead, they appear to be persistently generating upstream propagating waves.

Further evidence of the non-steady character of these flows is shown in the time series of the drag on the obstacle plotted in figure 16. For $K = 1.4$ and 1.5 the oscillations in the drag have quite large amplitude (which may even be increasing with time) and an approximately constant period. For $K = 1.6$, the period also appears to be constant, but the amplitude decays to a much smaller value after about $Ut/D \approx 25$, and remains at this smaller but non-zero amplitude thereafter. For $1.7 < K < 2.0$ (not shown), the drag behaved similarly to what was observed at $K = 1.6$. In general, we found that the period of these drag oscillations is mainly a function of K and only a weak function of the amplitude and horizontal lengthscale of the obstacle. The amplitude and mean value of the drag oscillations seem to depend more on the dimensions of the obstacle.

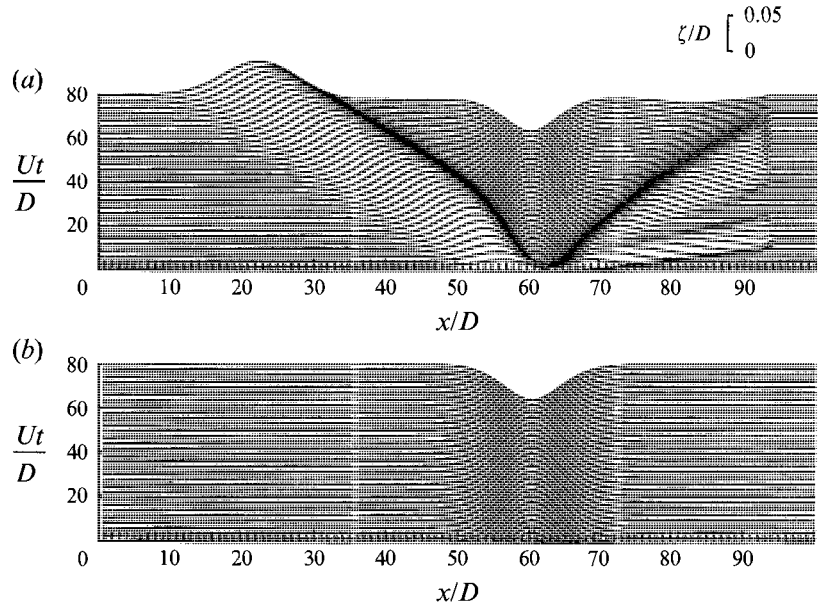

FIGURE 17. The evolution of the vertical displacement $\zeta(x, z, t)$ evaluated at mid depth, $z/D = 0.5$, for the case with $Ka/D = 0.1$, $L/D = 6.0$ and $K = 1.5$: (*a*) spectral model and (*b*) Long's model. The obstacle is centred at $x/D = 60$.

Also in figure 16 we have plotted the drag as computed from the GY model, for mode 1 waves, for all three cases. Even though these values of K are technically out of the range of validity of the FLW equation, the period of the drag oscillations is reproduced fairly well. On the other hand, the GY model computed drag seems to have a positive offset and, at least for $K = 1.4$, the oscillations decay much faster than in the spectral model.

We found that for large values of L/D, a steady-state solution is approached rapidly in the neighbourhood of the obstacle, and the steady solution approached in the spectral numerical simulation is indeed the steady solution of Long's model. An example of this kind of result is shown in figure 17(*a*). This plot shows the vertical displacement at mid-depth as a function of x and t for the case with $Ka/D = 0.1$, $L/D = 6.0$ and $K = 1.5$. It is clear in this plot that after the transients propagate away from the obstacle that a steady dip remains over the obstacle, as is predicted by the long-wave version of Long's model. This steady-state solution is plotted in figure 17(*b*) for convenient comparison.

Linear theory helps to explain the oscillatory behaviour of the solutions for sufficiently narrow obstacles. According to linear theory, the internal waves in a channel have a continuous spectrum in the horizontal with wavenumber k and a discrete spectrum in the vertical with wavenumbers m_n, which have the values,

$$m_n = n\pi/D \quad (n = 1, 2, \ldots), \tag{4.3}$$

where n is the mode number. In a reference frame in which the mean flow in the channel is zero, the horizontal phase speed c_n of these waves is given by

$$c_n(k) = \frac{N}{(k^2 + m_n^2)^{1/2}}, \tag{4.4}$$

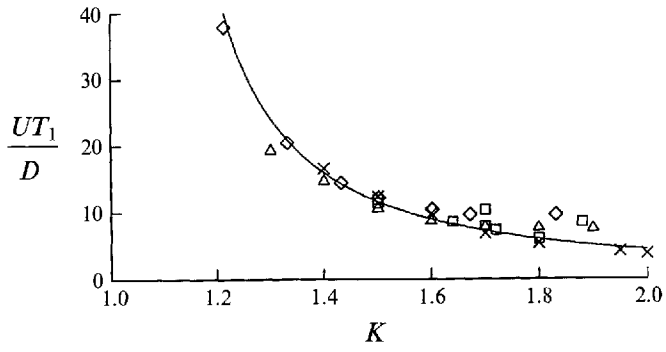

FIGURE 18. The period T_1 of the most persistent upstream propagating mode 1 wave based on linear theory for $1 < K < 2$ and comparison with the period of oscillation of the drag: ——, linear theory; □, Castro *et al.* (1990); ◇, Lamb (1994); △, Paisley *et al.* (1994); ×, present spectral model (for $Ka/D = 0.1$, $L/D = 1.0$). The Castro *et al.* data are from experiments using a vertical fence with height $a/D = 0.18$ or a Witch of Agnesi obstacle with $a/D = 0.10$, 0.20 and $L/D = 0.08$, 0.16. The Lamb data are for a Witch of Agnesi obstacle with $L/D = 0.17$. Lamb does not identify the obstacle amplitude, since he claims the period does not depend on it. The Paisley *et al.* data are for a vertical fence with height $a/D = 0.10$ and a Reynolds number of 100.

and the horizontal group speed γ_n by

$$\gamma_n(k) = \frac{Nm_n^2}{(k^2+m_n^2)^{3/2}}. \tag{4.5}$$

We seek the horizontal wavenumber k_n of the 'most persistent' wave; that is the wave that remains oscillating near the obstacle for the longest time. Such a wave should have a group speed equal in magnitude but opposite in direction to the oncoming flow speed U (and note that such a wave will have a horizontal phase speed with a magnitude that is greater than U). So, from (4.3) and (4.5) we derive,

$$k_n = \left[\left(\frac{K}{n}\right)^{2/3} - 1\right]^{1/2} m_n. \tag{4.6}$$

The period T_n of this most persistent wave then is given by

$$T_n = \frac{2\pi/k_n}{c_n(k_n) - U} = \frac{2}{n}\left[\left(\frac{K}{n}\right)^{2/3} - 1\right]^{-3/2} \frac{D}{U}. \tag{4.7}$$

We have plotted T_n as a function of K for $n = 1$ along with the measured periods of the drag oscillations from our spectral model simulations over the range $1 < K \leqslant 2$ in figure 18. The agreement between linear theory and our numerical simulations is very good.

Linear theory also helps explain why the oscillations are not observed for wide obstacles. In figure 19 we have plotted as a function of k the Fourier transform $\tilde{h}$ of our obstacle shape for two different widths: $L/D = 1$ and 2, and opposite this graph in the same figure we have plotted k_1 as a function of K. This figure is convenient for determining the magnitude of the Fourier transform of the obstacle at the 'most persistent' wavenumber for any specified value of K. For example, taking $K = 1.5$ we find the value of k_1 in the graph on the right and read across to the graph on the left to see that the obstacle transform has significant amplitude if $L/D \leqslant 1.0$ but is nearly zero if $L/D \geqslant 2.0$. Consequently, in an experiment or numerical simulation with K fixed, we may expect to see the oscillations in the drag for small L/D but not for large

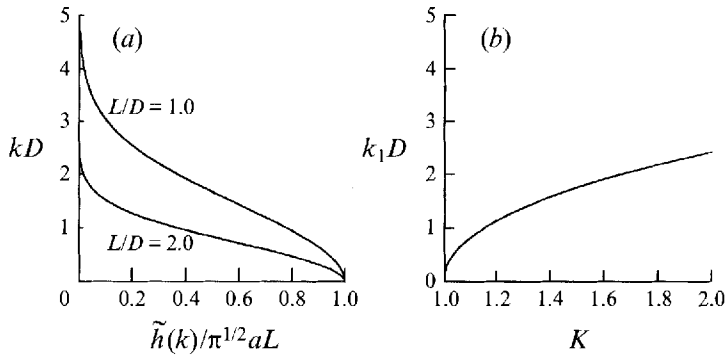

FIGURE 19. (*a*) The Fourier transform of the obstacle shape, $\tilde{h}(k)$, as a function of the horizontal wavenumber k for $L/D = 1.0$ and 2.0, and (*b*) the horizontal wavenumber k_1 of the most persistent mode 1 wave as a function of K, based on linear theory. Comparing (*a*) and (*b*) shows that when $K > 1.6$, or so, then in order for the most persistent wave to exist with any significant amplitude, we must have an obstacle with dimensions such that $L/D \leqslant 1.0$.

L/D. Looking at this another way, with L/D fixed, we might expect to see the amplitude of the oscillations in the drag to decrease as K is increased because k_n is an increasing function of K (for fixed mode number).

It is interesting that linear theory explains the period and the L/D dependence of the drag oscillations, even for internal wave amplitudes that are weakly nonlinear. However, linear theory also predicts that these oscillations should decay with the time dependence $t^{-1/2}$ and at least for some of the cases shown in figure 16 the oscillations seem more persistent than this. So nonlinearity apparently affects the persistence of the oscillations more than their period.

Lamb (1994) observed similar oscillations of the drag in his numerical simulations of inviscid stratified flow over topography when $1 < K < 2$. Lamb reported results on the period of the drag oscillations for flow over a Witch of Agnesi obstacle with half-width $L/D = 0.17$, which is substantially narrower than most of the obstacles we used in our simulations. He found, as we have, that the period is insensitive to the obstacle amplitude. We have plotted Lamb's values for the period in figure 18. Linear theory as well as our numerical simulations agree very well with most of Lamb's numerical simulations. The only significant discrepancy is that Lamb's values for the period seem to approach a constant ($\approx 9.8\, D/U$) as K approaches 2, whereas the values from our numerical simulations continue to decrease (reaching about $4.4\, D/U$ at $K = 2$) following the linear theory curve.

Castro, Snyder & Baines (1990) also observed persistent oscillations of the drag in their tow-tank experiments of uniformly stratified flow over obstacles. Several different obstacle shapes were used in these experiments: a two-dimensional fence with height $a/D = 0.2$ and two Witch of Agnesi obstacles with heights $a/D = 0.1$ and 0.2 and corresponding half-widths $L/D = 0.08$ and 0.16 (actually, it was the same Agnesi obstacle but with different values of D). Such narrow obstacles invariably produced boundary-layer separation in the lee of the obstacles which lead to an unsteady wake flow and associated mixing, something that cannot be reproduced in inviscid numerical simulations. Probably as a result of this, there are some significant differences between the results for the tow-tank experiments and the numerical simulations. First, persistent oscillations in the drag were observed in the experiments only when $1.4 < K < 2.0$ (in the experiments oscillations were also observed when $2.5 \leqslant K < 3.0$, but we are confining our attention here to $1 \leqslant K \leqslant 2$), whereas in the inviscid

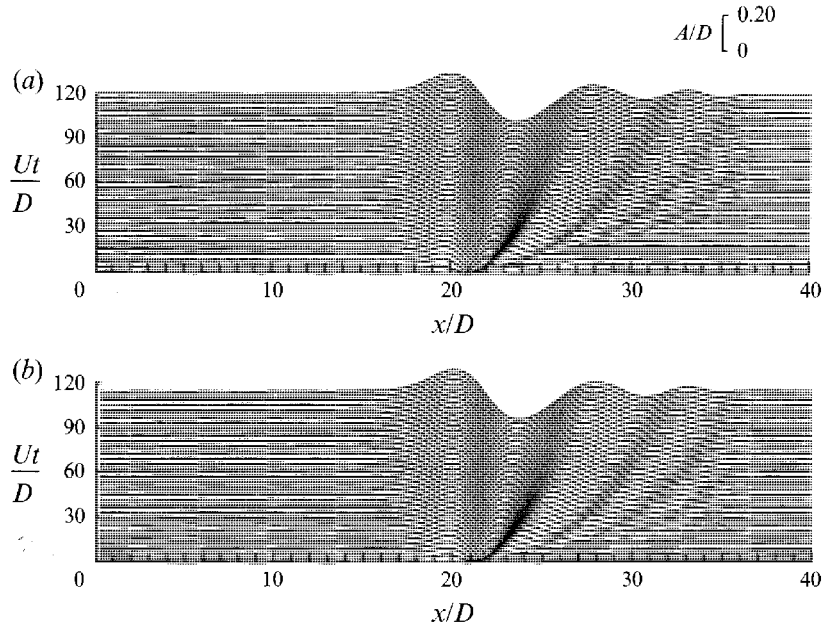

FIGURE 20. The amplitude function $A(x, t)$ for the resonant mode of the vertical displacement for the cases with $Ka/D = 0.1$, $L/D = 1.0$, and $K = 2.0$, (*a*) spectral model and (*b*) GY model. The obstacle is centred at $x/D = 20$.

numerical simulations oscillations were observed over the whole range $1.0 < K \leqslant 2.0$. Secondly, Castro *et al.* found that for fixed K the period had a weak dependence on the amplitude of the obstacle which is not seen in the numerical simulations. Despite these differences, we have plotted in figure 18 Castro *et al.*'s observed periods at values of K for which oscillations exist and find that they agree fairly well with linear theory and with the numerical simulations.

More recently, Paisley, Castro & Rockliff (1994) observed oscillations in the drag in their numerical simulations of viscous laminar flow of a uniformly stratified fluid over a vertical barrier. All these simulations were done with a barrier height of $a/D = 0.1$ and a Reynolds number of 100. They observed persistent oscillations in the drag for $1.3 \leqslant K \leqslant 1.6$ and decaying oscillations for $1.7 \leqslant K \leqslant 2.0$. We have plotted their results for the period of the drag oscillations in figure 18 and again the agreement with our inviscid numerical simulations and with linear theory is extremely good except near $K = 2.0$, where their periods appear to approach a constant value of about $7.7D/U$ instead of the linear theory result of about $4.4D/U$.

4.4. *The second resonance point* ($K = 2$)

In this section we describe our results of the parameter space in the vicinity of the second resonant point at $K = 2$. Again, using both the spectral model and the GY model we performed a large number of calculations for a variety of combinations of the flow parameters. Specifically, the range of flow parameters for which we performed calculations was: $0.05 < Ka/D < 0.2$ and $1.95 < K < 2/(1-2a/D)$. However, for brevity we will discuss only the cases with $K = 2$, plotted as □ in the parameter space in figure 3, since analogues of most of the conclusions reached in §4.2 also apply here.

Comparisons of the resonant amplitude function $A(x, t)$ at $K = 2$ as computed by both the spectral model and the GY model are shown in figure 20 for $L/D = 1.0$ and in figure 21 for $L/D = 2.0$. The evolution of these amplitude functions is shown up to

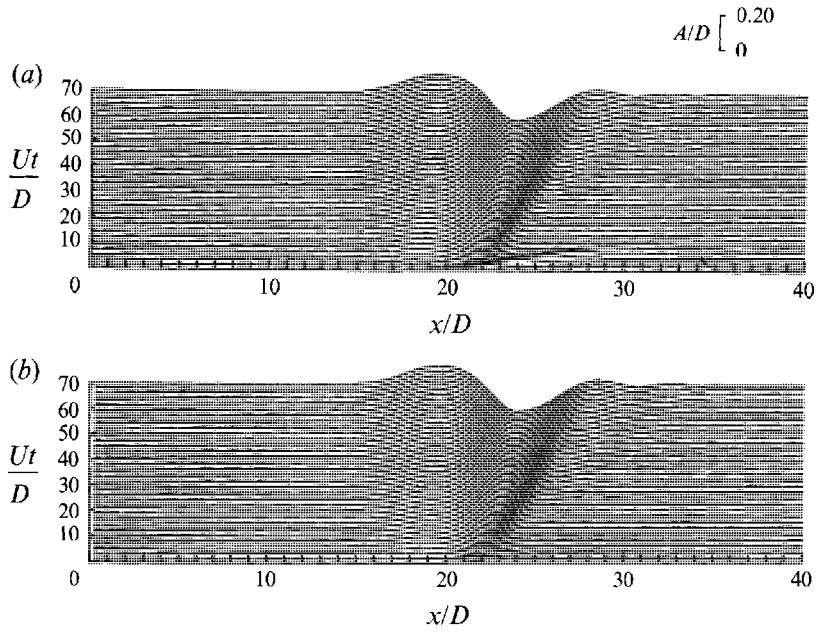

FIGURE 21. The amplitude function $A(x, t)$ for the resonant mode of the vertical displacement for the cases with $Ka/D = 0.1$, $L/D = 2.0$, and $K = 2.0$, (*a*) spectral model and (*b*) GY model. The obstacle is centred at $x/D = 20$.

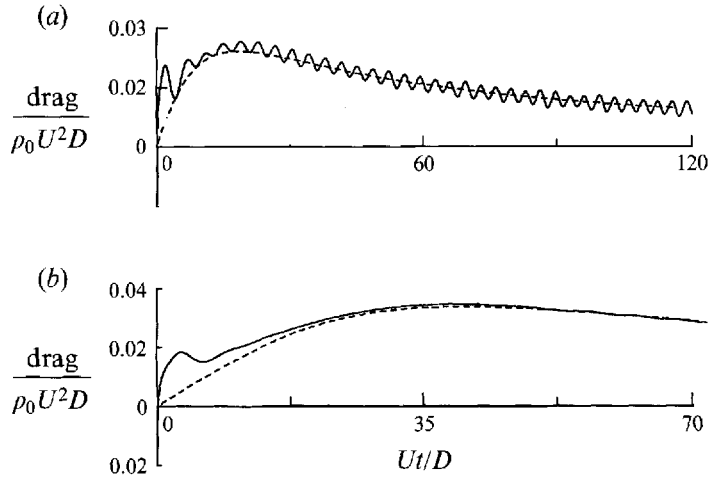

FIGURE 22. A plot of the drag as a function of time for the case with $K = 2.0$, $Ka/D = 0.1$ with (*a*) $L/D = 1.0$ and (*b*) $L/D = 2.0$: ——, spectral model; – – –, GY model.

the initial occurrence of wave breaking, which happens to be for the GY model. As was the case at the first resonance point, the wave-breaking time predicted by the GY model is about 25% short of the time predicted by the spectral model. Otherwise, in both cases the GY model reproduces the spectral model results very well.

Similar plots for the evolution of the first mode as computed by the spectral model (not shown) have the expected behaviour. For $L/D = 1.0$ a series of mode-1 waves propagate upstream while a fairly steady dip forms over the obstable, which is typical subcritical behaviour. There is some indication of periodic unsteadiness due to the

continuous series of upstream propagating waves. For $L/D = 2.0$, the situation is much the same except that only one mode-1 wave propagates upstream and after that wave leaves the vicinity of the obstacle the dip that forms over the obstacle is very steady.

We have plotted the time series for the drag as computed by the spectral model and the GY model for $L/D = 1.0$ and 2.0 in figure 22. For $L/D = 1.0$ (figure 22*a*), the spectral model produces a drag that has the same mean time evolution as the GY model, but it has a persistent oscillation about the mean that does not appear in the GY calculation. These oscillations, due to mode 1 waves, are similar to what we described earlier in §4.3, except the oscillations at $K = 2.0$ are weaker and follow a more strongly non-zero mean. For $L/D = 2.0$ as shown in figure 22(*b*), the oscillations in the drag are greatly reduced and the GY calculation is an excellent approximation to the fully nonlinear calculations. By analogy with the results at $K = 1$, we would expect the drag in the present cases to asymptote to a small positive value. However, extending these calculations much further in time, we find that the drag continues to decline although at a very slow rate. As best we can tell the drag in the present cases either asymptotes to a very small positive value or zero.

For $L/D \gg 1$, we find that the wave-breaking times as computed by the spectral model are described well by the empirical formula (4.1) with $n = 2$.

5. Summary and conclusions

We have reported numerical results for the flow in a channel of a uniformly stratified Boussinesq fluid over isolated bottom topography. We used a spectral model to solve the fully nonlinear inviscid two-dimensional equations, with the flow impulsively started from rest. For comparison, we have integrated numerically the finite-amplitude long-wave (FLW) evolution equation derived by GY. We have restricted attention to obstacles of small to moderate amplitude and slope and to values of K near or between the resonances at $K = 1$ and $K = 2$. We did not make a concerted effort to verify the shape of the hydrostatic 'breaking curve' (2.20) over the entire range $1 \leqslant K \leqslant 2$. However, we did find that for sufficiently long hills in the neighbourhood of the resonant points the breaking curve accurately delineates the regions of the parameter space where breaking would and would not occur.

Near $K = 1$, the time to wave breaking (if it occurs), which is an indication of how rapidly the flow develops, was studied in detail as a function of K and the dimensions of the obstacle. For example (see figure 14), when $L/D \gg 1$ our results show that wave breaking occurs at non-dimensional times that are proportional to L/a. However, when $L/D \ll 1$, our results indicate that the wave-breaking time is inversely proportional to $(a/D)^3(L/D)^3$. The constants of proportionality are functions of K. The wave-breaking times for these two limiting regimes follow the scaling derived from linear resonant theories that apply to these two limiting cases. Comparisons between our spectral model and GY show close agreement in most cases, even for obstacles of relatively large amplitude. The poorest agreement is found for small L/D and the best agreement for $L/D \approx 1$. For $L/D > 1$, the GY theory predicts faster wave-breaking times than our spectral model, but the difference is generally less than 25%.

The agreement between our spectral model and GY is best when the obstacle dimensions satisfy the KdV scaling relationship on which the GY theory is based: $D/L \sim (a/D)^{1/2}$. With the additional constraint that the obstacle amplitude be small, this scaling restricts the applicability of the FLW equation to obstacles with small to moderate slopes.

For values of K near 1.5, we find that the steady non-resonant solutions of Long (1955) are achieved for sufficiently long obstacles. For narrower obstacles, we observe oscillations about the predicted steady state which continue for very long times. The amplitude of the oscillations depends on the amplitude and slope of the obstacle as well as on K, but the period depends mainly on K. We offer an explanation for these oscillations using linear theory for the most persistent internal waves that are generated by narrow obstacles but not by long ones. The oscillations also appear in the numerical simulations of Lamb (1994) and Paisley *et al.* (1994) and in the tank experiments of Castro *et al.* (1990), although in the latter there is some dependence of the period of oscillation on the amplitude of the obstacle.

Near the resonance at $K = 2$ we find similar behaviour to that near the resonance at $K = 1$, except for the presence of small-amplitude mode-1 internal waves, which appear near the obstacle when the obstacle is sufficiently narrow. Again, except for these mode-1 internal waves, the GY solution accurately reproduces many of the main features of the flow obtained by the spectral model for obstables that are not too narrow.

We acknowledge helpful discussions with Simon Clarke about the modal similarity properties of the FLW equation. We are grateful to Marina De Gabriele for her help with the numerical simulations and with the preparation of the figures. This research was partially supported by ARC Grant A8923061. J.W.R. acknowledges additional financial support from NASA Contract W-18,566.

REFERENCES

BAINES, P. G. 1977 Upstream influence and Long's model in stratified flows. *J. Fluid Mech.* **82**, 147–159.

BAINES, P. G. & GUEST, F. 1988 The nature of upstream blocking in uniformly stratified flow over long obstables. *J. Fluid Mech.* **188**, 23–45.

BOYD, J. P. 1989 *Chebyshev and Fourier Spectral Methods*. Springer.

CANUTO, C., HUSSAINI, M. Y., QUARTERONI, A. & ZANG, T. A. 1988 *Spectral Methods in Fluid Dynamics*. Springer.

CASTRO, I. P., SNYDER, W. H. & BAINES, P. G. 1990 Obstacle drag in stratified flow. *Proc. R. Soc. Lond.* A **429**, 119–140.

GRIMSHAW, R. H. J. & SMYTH, N. 1986 Resonant flow of a stratified fluid over topography. *J. Fluid Mech.* **169**, 429–464.

GRIMSHAW, R. H. J. & YI ZENGXIN 1991 Resonant generation of finite-amplitude waves by the flow of a uniformly stratified fluid over topography. *J. Fluid Mech.* **229**, 603–628.

HANAZAKI, H. 1989 Upstream advancing columnar disturbances in two-dimensional stratified flow of finite depth. *Phys. Fluids* A **1**, 1976–1987.

HANAZAKI, H. 1992 A numerical study of nonlinear waves in a transcritical flow of stratified fluid past an obstacle. *Phys. Fluids* A **4**, 2230–2243.

HANAZAKI, H. 1993 On the nonlinear internal waves excited in the flow of a linearly stratified Boussinesq fluid. *Phys. Fluids* A **5**, 1201–1205.

LAMB, K. G. 1994 Numerical simulations of stratified inviscid flow over a smooth obstable. *J. Fluid Mech.* **260**, 1–22.

LONG, R. R. 1955 Some aspects of the flow of stratified fluid. III. Continuous density gradients. *Tellus* **7**, 341–357.

PAISLEY, M. F., CASTRO, I. P. & ROCKLIFF, N. J. 1994 Steady and unsteady computations of strongly stratified flows over a vertical barrier. In *Stably Stratified Flows: Flow and Dispersion over Topography* (ed. I. P. Castro & N. J. Rockliff), pp. 39–59. Clarendon.

YI ZENGXIN & WARN, T. 1987 A numerical method for solving the evolution equation of solitary Rossby waves on a weak shear. *Adv. Atmos. Sci.* **4**, 43–54.